ADVANCED FUNCTIONAL MATERIALS
www.afm-journal.de

Buffer Layer Stabilized Single-Unit Cell Ferroelectric Bi_2TeO_5

Yunfei Li, Alei Li, Cong Wang, Mengjiao Han, Juntong Zhu, Yunlei Zhong, Pin Zhao, Ge Song, Shun Wang, Zongjie Shen, Lin Wang, Hui Zhang, Wu Zhou, Lu You, Wei Ji,* Junhao Lin,* and Lixing Kang**

Miniaturizing van der Waals (vdW) ferroelectric materials to atomic scales is essential for modern devices like nonvolatile memory and sensors. To unlock their full potential, their growth mechanisms, interface effects, and stabilization are preferably investigated, particularly for ultrathin 2D nanosheets with single-unit cell thickness. This study focuses on Bi_2TeO_5 (BTO) and utilizes precise control over growth kinetics at the nucleation temperature to create specific interfacial reconfiguration layers. Ultrathin BTO nanosheets with planar ferroelectricity at a single-unit cell thickness are successfully grown. Atomic-scale characterization reveals a disordered distribution of elements in the interfacial layer, which buffers strain from lattice mismatch. The theoretical calculations support these observations. Furthermore, this strategy also can be extended to the growth of a variety of 2D ternary oxide nanosheets. This work contributes to a better understanding of growth and stability mechanisms in 2D ultrathin nanosheets.

1. Introduction

In the field of contemporary nanoelectronics, van der Waals (vdW) ferroelectric materials are celebrated for their unique physical properties such as a dangling-bond-free surface, tunable interfaces, thickness, and band structure.[1–5] These characteristics enable significant potential in technologies like low-dimensional field-effect transistors, nanoscale low-power logic devices, and non-volatile memory.[6–10] However, to achieve high integration and low power consumption in electronic devices, precise control over the thickness and ferroelectric properties of these materials is critical, especially to maintain stable ferroelectric performance at ultra-thin levels. Therefore, the synthesis and stabilization of ferroelectric materials with thicknesses down to a single-unit cell are essential for future high-density electronic circuit applications.

Significant efforts have been devoted to developing ultra-thin ferroelectric materials that remain stable even at the thickness of a single-unit cell. Mechanical exfoliation has emerged as a successful technique for producing such materials, including monolayers like $CuInP_2S_6$,[11] GaSe,[12] and

Y. Li, L. Kang
School of Nano-Tech and Nano-Bionics
University of Science and Technology of China
Hefei 230026, China
E-mail: lxkang2013@sinano.ac.cn

Y. Li, A. Li, Y. Zhong, P. Zhao, G. Song, Z. Shen, L. Wang, H. Zhang, L. Kang
Division of Advanced Materials
Suzhou Institute of Nano-Tech and Nano-Bionics
Chinese Academy of Sciences
Suzhou 215123, China

C. Wang, W. Ji
Beijing Key Laboratory of Optoelectronic Functional Materials & Micro-Nano Devices
Department of Physics
Renmin University of China
Beijing 100872, China
E-mail: wji@ruc.edu.cn

C. Wang, W. Ji
Key Laboratory of Quantum State Construction and Manipulation (Ministry of Education)
Renmin University of China
Beijing 100872, China

M. Han
Bay Area Center for Electron Microscopy
Songshan Lake Materials Laboratory
Dongguan, Guangdong 523808, China
E-mail: hanmengjiao@sslab.org.cn

J. Zhu, W. Zhou
School of Physical Sciences
CAS Key Laboratory of Vacuum Physics
University of Chinese Academy of Sciences
Beijing 100049, China

S. Wang, L. You
School of Physical Science and Technology
Jiangsu Key Laboratory of Thin Films
Soochow University
Suzhou 215006, China

J. Lin
Department of Physics and Shenzhen Key Laboratory of Advanced Quantum Functional Materials and Devices
Southern University of Science and Technology
Shenzhen 518055, China
E-mail: linjh@sustech.edu.cn

The ORCID identification number(s) for the author(s) of this article can be found under https://doi.org/10.1002/adfm.202421384

DOI: 10.1002/adfm.202421384

1T-$MoTe_2$.[13] However, achieving a thickness equivalent to a single-unit cell in current ferroelectric materials remains a challenge. Moreover, even when achievable, the production process is inefficient and costly. In contrast, methods such as chemical vapor deposition (CVD) and physical vapor deposition (PVD) enable the efficient fabrication of ferroelectric materials with a controllable thickness,[14] such as monolayer SnS,[15] few-layer In_2Se_3[16,17] and $CuCrSe_2$.[18] Nevertheless, the materials produced typically range to several unit cell thicknesses, and due to size effects, the ferroelectric properties can be suppressed or even lost when the thickness is reduced to the nanoscale, leading to compromised stability.[19,20] In recent years, it has been found that the size effect can be mitigated through strategies such as strain engineering, doping to alter the chemical environment and careful selection of substrates. For instance, doping HfO_2 with La or Y,[21] and using Sm in $Bi_{1.8}Sm_{0.2}O_3$ through chemical epitaxy,[22] preserves their ferroelectricity at smaller scales, while strain and size reduction enhance the properties in $Hf_{0.8}Zr_{0.2}O_2$,[23] $BiFeO_3$,[24] and sub-nanometer ZrO_2 films.[25] However, this approach is currently constrained to non-layered ferroelectric materials, which poses challenges in achieving epitaxial growth and high functional integration. Consequently, a pressing need exists for a universal approach to acquire and stabilize vdW ferroelectric materials down to single-unit cell thickness. Investigating the potential applicability of single-layer ferroelectric stabilization strategies from traditional materials to vdW ferroelectric materials holds significant promise.

In previous work, we controlled the ratio of Bi and Te elements and utilized chemical vapor deposition to fabricate BTO nanosheets with in-plane ferroelectricity and to manipulate in-plane ferroelectric domains. To achieve the growth of ferroelectric nanosheets with a single-unit-cell thickness, this work introduces a customized buffer layer approach to control the layered epitaxial growth of Bi_2TeO_5 (BTO).[26] By maintaining a constant Bi/Te ratio and adjusting nucleation sites for growth, we achieved single-unit cell monocrystalline BTO nanosheet growth using a disordered elemental bismuth tellurite (DEBT) buffer layer. Combining nonlinear optics, piezoelectric force microscopy (PFM), aberration-corrected scanning transmission electron microscopy (STEM), and first-principles calculations, we elucidate the intrinsic in-plane ferroelectricity and stabilization mechanism of single-unit cell thickness BTO nanosheets. The DEBT buffer layer, characterized by disordered chemical element distribution, effectively mitigates strain with the mica substrate, facilitating the nanosheets to achieve a perfect lattice and stabilize intrinsic in-plane ferroelectricity at the BTO monolayer. Furthermore, BTO nanosheets exhibit potential for planar ferroelectric devices. Our findings contribute novel insights into the growth of ultrathin oxide nanosheets and strategies for stabilizing ultrathin ferroelectrics.

2. Results and Discussion

2.1. Controlled Synthesis of Ultrathin BTO Nanosheets

In our previous report, we demonstrated that by adjusting the ratio of Bi/Te elements, the in-plane transverse elemental distribution of BTO nanosheets can be controlled to produce ferroelectric or antiferroelectric nanosheets with tunable domain wall dimensions.[26] In contrast, we found that the vertical growth of BTO nanosheets at a relatively fixed Bi/Te ratio also exhibits a very interesting growth mode. **Figure 1a** demonstrates a one-step CVD method for DEBT buffer layer coverage and epitaxy of a single crystalline layer by adjusting the growth parameters control strategy. At a lower temperature, BTO first forms a buffer layer on the (001) surface of fluorocrystalline mica substrates, which shown in step 1 and step 2 in Figure 1a. The DEBT buffer layer, which generally has single- or two-unit cell thicknesses, reduces the lattice mismatch between the substrate and the single-crystal nanosheets, while simultaneously providing additional nucleation sites, which are conducive to the epitaxial growth of monolayer single-crystal BTO nanosheets. By adjusting the nucleation time, homogeneous epitaxial growth of single cell-thickness BTO nanosheets with high crystallinity was achieved through the spontaneous formation of buffer layers in step 3 in Figure 1a. A representative optical image of just DEBT buffer layer and DEBT buffer layer-BTO nanosheets as grown on a mica substrate could be seen in Figure 1b,c.

The growth parameters significantly influence the growth of BTO single-crystal nanosheets. Initially, the DEBT buffer layer can be obtained by growing at a lower temperature (500 °C) for 2 min, depicted in Figure S1 (Supporting Information), which is generally quasi-circular with signs of a second layer in the middle, and the height is typically one- or two-unit cell thicknesses (Figure 1b and Figure S2, Supporting Information) The formation of the buffer layer may be due to the kinetic limitations of gas molecules diffusing on the substrate at lower temperatures, preventing the film from achieving complete crystallization or order.[27–29] This low-temperature epitaxial buffer layer technique is commonly used in the epitaxial growth process of 3D semiconductors to address the lattice mismatch between the environmental substrate and the epitaxial layer.[30,31] Subsequently, by increasing the growth temperature (550–600 °C), further epitaxial growth of nanosheets with a single-crystal structure on the buffer layer is enabled, gradually transforming their shapes into rectangles (Figure 1c). Optical microscopy (OM) images of single-crystal 2D BTO nanosheets are shown in Figure 1e, while atomic force microscopy (AFM) characterization is demonstrated in the inset of Figure 1e. With further extension of the growth time, the buffer layer was all transformed into rectangular BTO nanosheets, and the thickness of the nanosheets increased with the growth time, as shown in Figure 1f. When the buffer layer strategy is not used, as shown in Figure S3 (Supporting Information), the BTO nanosheets fail to achieve layered epitaxial growth. The growth temperature needs to reach 680 °C, and the resulting films exhibit greater thickness and uneven morphology, which is consistent with the observations in our previous work.[26] The crystal structure of the ultrathin BTO nanosheets is confirmed using X-ray diffraction (XRD) as shown in Figure S4a (Supporting Information), where the detected signals correspond to the (312) crystal planes of tetragonal Bi_2TeO_5.[32]

Furthermore, the Raman spectrum of BTO nanosheets deposited on the SiO_2/Si substrate is depicted (Figure S5, Supporting Information). Our CVD-processed BTO nanosheets exhibit a dominant peak around 760 cm^{-1}, along with peaks at 661 cm^{-1}, 219 cm^{-1}, and 111 cm^{-1}, which closely correspond to the Raman peaks reported for single-crystal BTO.[33] In the low-frequency range below 150 cm^{-1}, the observed peak at 111

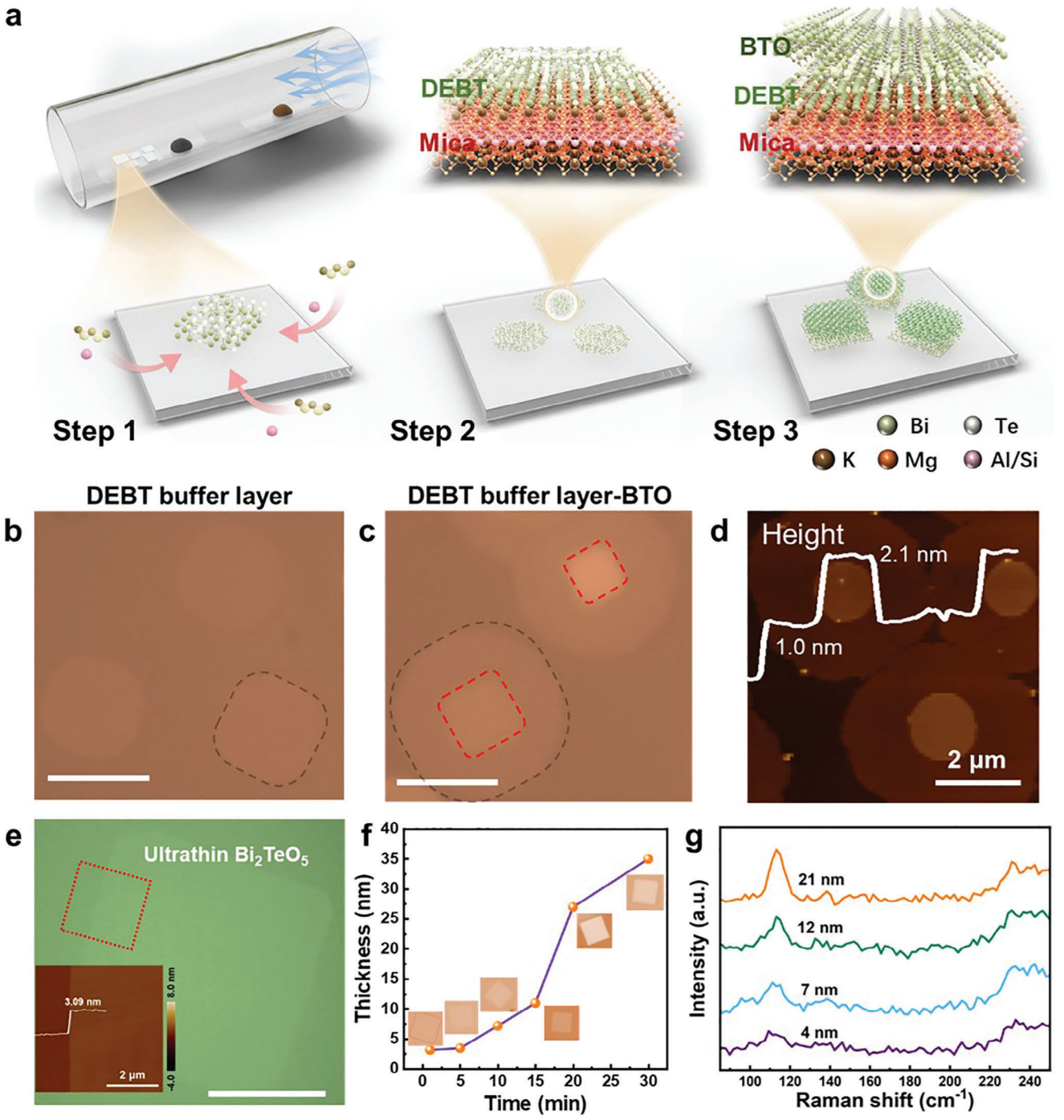

Figure 1. Schematic illustration of the buffer layer control strategy toward the synthesis of monolayer BTO nanosheets. a) Schematic of DEBT-BTO synthesis processes. By adjusting the growth rate, a DEBT buffer layer was first obtained on mica, and then a single layer of monocrystalline BTO nanosheets could be obtained by epitaxy on it. b) A representative optical image of just DEBT buffer layer and c) DEBT buffer layer-BTO nanosheets as grown on a mica substrate. Scale bar 15 μm. d) The AFM height image of DEBT buffer layers. e) OM image of a BTO ultrathin nanosheet and corresponding AFM image of the red-dashed box. Scale bar, 10 μm. f) Statistical thickness of BTO nanosheets synthesized at different growth times. Insets are the corresponding typical OM images. g) Raman spectrum of BTO nanosheets with different thicknesses, which shows a positive correlation between thickness and the strength of A_{1g} mode.

cm^{-1} in our BTO nanosheets is associated with the bending vibrations of the Bi—O—Bi, Bi—O—Te, and Te—O—Te bonds.[34] The intensity of the 111 cm^{-1} which is attributed to Te—O—Te band as shown in Figure 1g is positively correlated to the thickness of BTO. The photoluminescence (PL) emission was also conducted to reveal the bandgap of the BTO nanosheets. Figure S4b (Supporting Information) illustrates a broad PL spectrum peak at 528 nm observed from the 2D BTO nanosheets when excited with 355 nm wavelength, which indicated a big optical bandgap of ≈2.35 eV for BTO.[35] The elemental composition and bonding type of BTO nanosheets were analyzed using X-ray photoelectron spectroscopy (XPS). In Figure S6a (Supporting Information), peaks centered at 159.0 and 164.3 eV are attributed to Bi $4f_{7/2}$ and Bi $4f_{5/2}$ in bismuth oxide, respectively. The XPS spectrum of Te exhibits signals at 575.4 and 585.9 eV as shown in Figure S6b (Supporting Information), corresponding to Te $3d_{5/2}$ and Te $3d_{3/2}$ with a valence state of -2. The O 1s spectrum shows two peaks centered at 529.5 and 531.6 eV in Figure S6c (Supporting Information). These findings indicate that the as-grown BTO nanosheets possess high quality and an ideal stoichiometric ratio.

2.2. DEBT Buffer Layer with Random Chemical Distribution

As shown in **Figure 2**a, we can visualize the whole growth process from the interface, where DEBT acts as a buffer layer and plays an important part between the mica and the ultrathin BTO nanosheets. To further investigate the chemical composition of the DEBT buffer layer and its role in the growth of BTO nanosheets. We used high-angle annular dark field scanning transmission electron microscopy (HADDF-STEM) to probe the elemental distribution of BTO samples with different layers. Due to the special growth mechanism of BTO, the DEBT buffer layer is defined as the layer within two-unit cells of thickness, transitioning to crystallized BTO nanosheets from the third-unit cells onward. For the layered, asymmetric orthorhombic BTO crystal, the unit cell thickness along the c-axis is 1.17 Å, which corresponds to the thickness of a single BTO layer (Figure S7, Supporting Information). Since the thickness of a BTO monolayer corresponds to the thickness of one unit cell along the c-axis, we refer to DEBT and BTO nanosheets with a single unit cell thickness as monolayers, and those with two unit cell thicknesses as bilayers, and so on. Figure S8 (Supporting Information) shows the HAADF-STEM images of the samples with DEBT monolayer, DEBT bilayer, BTO monolayer, and BTO bilayer, respectively. It is clearly seen that the BTO monolayer and bilayer can maintain better lattice periodicity, and the Bi^{3+} and Te^{2+} are canonically arranged in a lattice array of dots, which indicates the stability of the atomic layers. When the thickness of nanosheets decreases to one-unit cell (DEBT monolayer), the lattice stripe arrangement is destroyed (Figure 2b,c). Besides, since there are at most two atoms in one column in single layer BTO, by using the contrast in HAADF-STEM images, the elements of each column can be determined, as shown in Figure 2d. The reconstructed structure shows that Bi and Te atoms are irregularly arranged in the lattice dot matrix, which makes it difficult to maintain a good lattice periodicity. Analysis of chemical elemental distributions reveals that Bi and Te are present in nonstoichiometric ratios, indicating a random distribution of these elements. Despite the same framework with BTO structure, Fast Fourier Transformation (FFT) and EDS statistics show a disappearance of superspots and a clear Bi deficiency in the DEBT monolayer, indicating randomly distributed elements in the buffer layer (Figure S9, Supporting Information).

Subsequently, the atomically resolved side-view HADDF-STEM images were used to further elaborate the atomic distribution of the DEBT and BTO nanosheets, as shown in Figure 2e,f. By analyzing the intensities in HAADF-STEM images, the elemental species of each line profile in different layers in Figure 2f were speculated, as shown in Figure 2g. It is clear that the chemical distribution along the *c*-axis appeared to be changing with increasing layers. The distributions of Bi^{3+} and Te^{2+} were irregularly distributed at the DEBT monolayer and bilayer only. With increasing thickness of the nanosheets to three-unit cells and more, the Bi^{3+} and Te^{2+} were distributed to conform to the periodic crystal structure as in BTO. As mentioned earlier, we define a layered structure with a disordered distribution of chemical elements in the thickness of the single- and two-unit cell thickness layers as a DEBT buffer layer. Above the DEBT buffer layer, a single crystalline BTO monolayer forms. We proposed that it is the DEBT buffer layer with a non-stoichiometric ratio of two-unit cell thicknesses that allows the nanosheets to exhibit a perfect lattice structure in the third layer (three-unit cell thicknesses), which means that the BTO monolayer can be stabilized.

2.3. Determination of the Ferroelectricity of the DEBT Buffer Layer and BTO Nanosheets

The symmetry of our DEBT buffer layer and BTO nanosheets was further explored using nonlinear optical second-harmonic generation (SHG). This technique is particularly relevant since ferroelectric polarization typically requires a broken inversion symmetry. It has been established that BTO crystallizes in the non-centrosymmetric space group Aem2, indicating its potential for ferroelectric properties. The SHG is a nonlinear optical phenomenon where two low-frequency photons interact with a nonlinear material, producing a photon with twice the frequency, as depicted in **Figure 3**a. Figure 3b displays the power-dependent SHG spectrum of BTO using an excitation wavelength of 1064 nm. Furthermore, the power-dependent SHG intensity demonstrates an effective fit to a logarithmic slope of 1.92 (Figure 3c), which closely approaches the theoretical value of 2 expected for second-order nonlinear processes. Since polarization-resolved SHG is contingent on crystal symmetry, we conducted angle-dependent SHG intensity measurements of the 2D non-layered Bi_2TeO_5 nanosheets. As demonstrated in Figure 3d, we explored the azimuthal angle-dependent SHG intensity by rotating the substrate around the incident direction of the laser. The angle-dependent SHG intensity demonstrates a symmetric pattern resembling two petals, modeled by the equation $I = I_0\cos^2(\theta + \theta_0)$, where I represents the SHG intensity, I_0 is the maximum SHG intensity, and θ_0 adjusts for the initial orientation of the sample. The SHG signals were characterized in nanosheets of various thicknesses to determine noncentrosymmetry, which is required for ferroelectricity. Figure 3e indicates SHG signals originate from nanosheets with at least 4 nm thickness, with intensity increasing with thickness. SHG tests were also conducted on

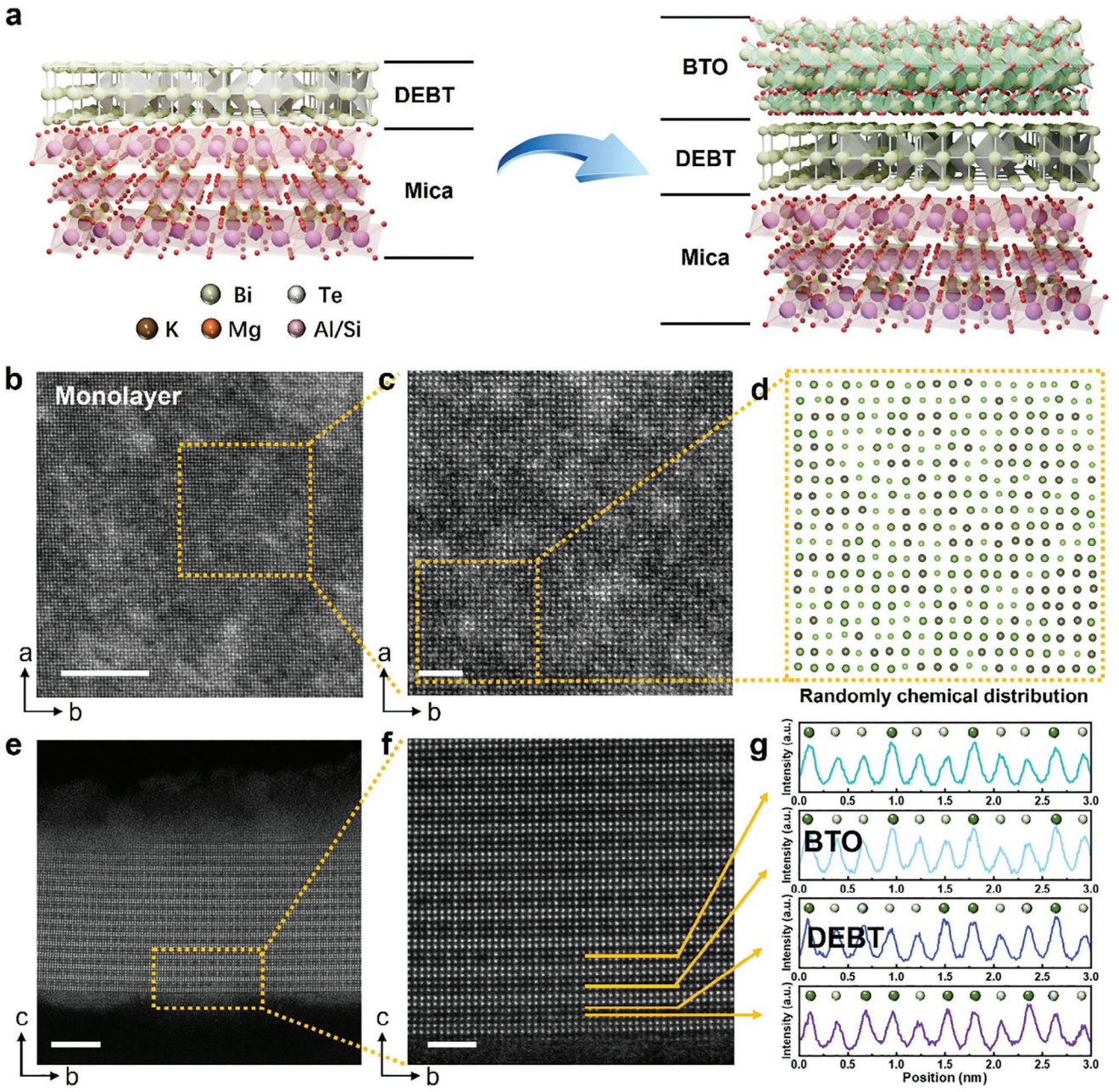

Figure 2. The elemental composition of DEBT buffer layer and BTO nanosheets. a) Schematic of lattice stacking of Mica-DEBT-BTO. b–d) Atomically resolved HAADF-STEM images of DEBT along the *c*-axis and corresponding lateral distribution of elements in the yellow boxed area. Scale bar in (b), 2 nm. e) The side-view HAADF-STEM image of DEBT and BTO nanosheet. Scale bar, 5 nm. f) Atomically resolved HAADF-STEM images of DEBT and BTO along the *b*-axis in the yellow boxed area in (e). Scale bar, 2 nm. g) The corresponding line profile in (g) along the *c*-axis shows the elemental distribution in the DEBT monolayer, DEBT bilayer, BTO monolayer, and BTO bilayer.

DEBT buffer layers with thicknesses of single-unit cells, which did not exhibit a significant signal, as shown in Figure 3f. These layers exhibited negligible SHG signals, even during polarization tests at arbitrary angles, in contrast, significantly stronger SHG signals were detected in thicker BTO nanosheets (Figure S10, Supporting Information). We also performed SHG testing on mica, which showed no signal, thus eliminating any influence from the substrate, as shown in Figure S10c,d (Supporting Information). Since SHG is sensitive to the symmetry of the crystal structure, the results indicate that nanosheets with one- and two-unit buffer layers have different lattice periodicity and symmetry than nanosheets with a third-layer thickness, distinguishing the one- and two-unit buffer layers from regular nanosheets using SHG.

PFM measurements were also used to investigate the ferroelectricity in BTO.[36] Figure 3g displays the AFM height and

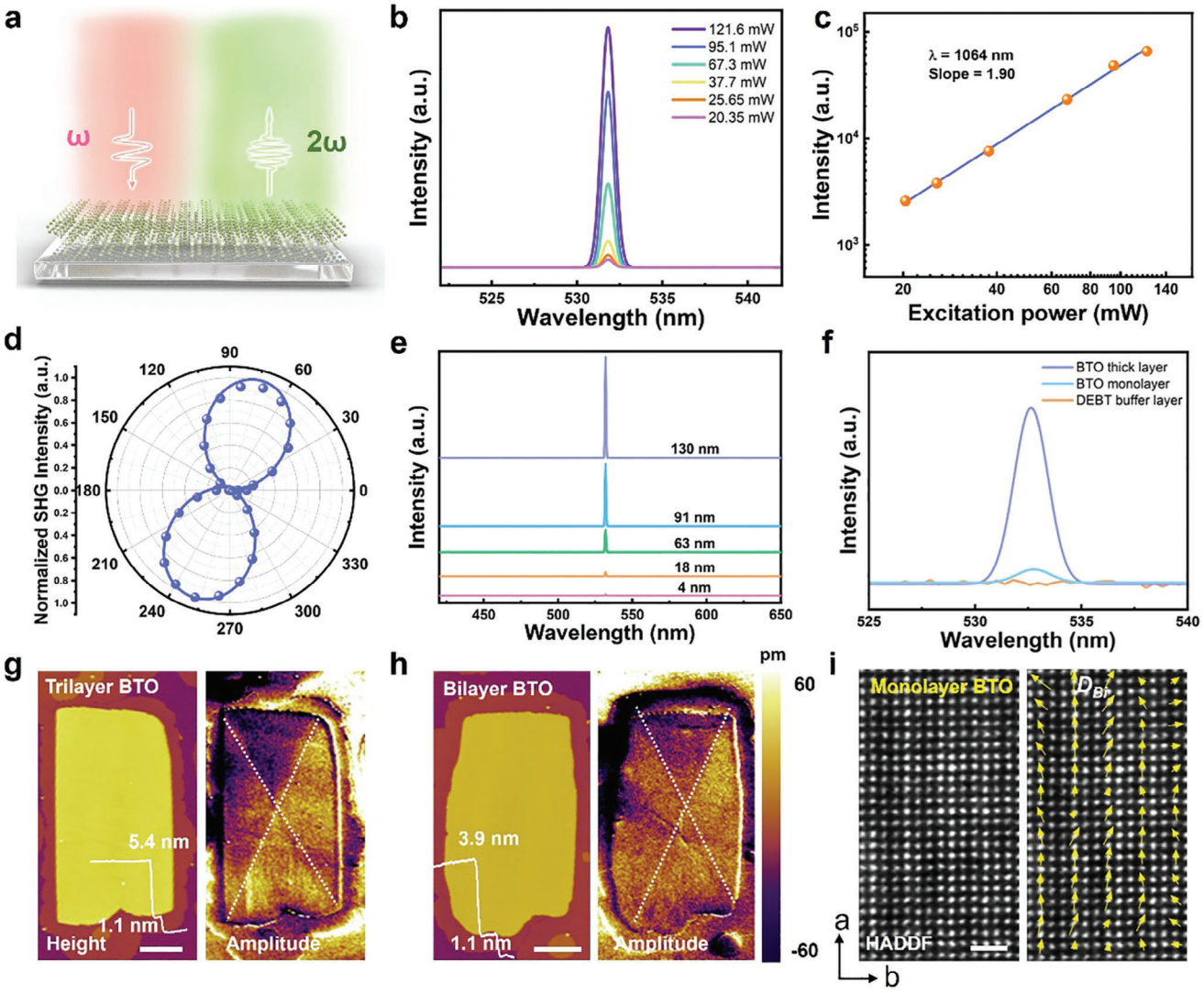

Figure 3. Determination of the ferroelectricity of DEBT buffer layer and BTO nanosheets. a) Schematic diagram of SHG measurement. b) Power-dependent SHG spectra, and c) the corresponding linear fitting in logarithmic coordinates. d) A typical polarization-resolved SHG spectra of BTO nanosheets. e) Thickness-dependent SHG of BTO nanosheets f) SHG spectra of the DEBT buffer layer, BTO monolayer, and BTO thick layer. g) Height and PFM amplitude images of trilayer and h) bilayer BTO nanosheets. The white lines in height images demonstrate the height profile of BTO nanosheets. The white dotted lines in amplitude images demonstrate the four triangle-shaped domains in BTO nanosheets. Scale bar 2 μm. i) HAADF-STEM image and corresponding Bi^{3+} displacements (D_{Bi}) in monolayer BTO. The yellow arrows denote the upward polarizations of Bi^{3+} cations. Scale bar 1 nm.

corresponding lateral amplitude images of a trilayer BTO nanosheet. The height image shows that a 1.1 nm step corresponds to the thickness of a single DEBT monolayer, while a 5.4 nm step indicates the combined thickness of one DEBT monolayer and three BTO layers. The lateral amplitude image shows a pattern of four triangular domains, delineated by white dashed lines in Figure 3g. Similar domain configurations are observable in the BTO bilayer, as depicted in Figure 3h. Phase information for the BTO trilayer and bilayer is shown in Figure S11a,b (Supporting Information), respectively. The thicker BTO sample, as seen in Figure S11c (Supporting Information), exhibits more clearly defined ferroelectric domains. Additionally, we observed typical PFM phase hysteresis loops and amplitude loops on the BTO nanofilms, providing strong evidence for the in-plane ferroelectricity of the BTO nanosheets (Figure S12, Supporting Information). The BTO monolayer is also capable of sustaining its ferroelectric polarization. This is further demonstrated by the atomic-resolution HAADF-STEM images and the calculated positional displacements of the BTO monolayer, shown in Figure 3i. These images highlight the upward polarization direction of Bi^{3+} cations, indicated by yellow arrows. However, ferroelectric domains were not observed in the DEBT monolayer and bilayer. (Figure S13, Supporting Information), consistent with the absence of SHG signals in DEBT monolayer and bilayer nanosheets mentioned earlier, while significant polarization was evident in BTO monolayers. From this, we can conclude that BTO grown by the DEBT buffer layer strategy have spontaneous polarization at single-unit cell thickness. Our previous work reported that

by tuning the Bi/Te ratio of BTO nanosheets, it is possible to confine their ferroelectric domains to a single-unit cell width.[26] This study explores whether such confinement persists vertically, specifically in ferroelectrics of single-unit cell thickness. Consequently, we have successfully prepared ternary oxide nanosheets with in-plane ferroelectricity in a single-unit cell thickness using a buffer layer strategy.

Furthermore, to gain a deeper understanding of the ferroelectric properties of BTO, we fabricated lateral two-terminal devices. These devices were utilized to showcase the potential memristor applications of BTO, leveraging its ferroelectric polarization switching capabilities. The preparation of BTO nanosheet transverse devices was performed directly on mica substrates, where two parallel Cr/Au electrodes were deposited as source and drain, as illustrated in Figure S14a (Supporting Information). The Kelvin probe force microscope (KPFM) image (Figure S15, Supporting Information) reveals a contact potential barrier approximately 60 meV greater than that of the gold substrate. Furthermore, chromium (Cr) was selected as the electrode material due to its comparatively lower work function of 4.5 eV. Therefore, establishing Schottky contact is established at the metal/semiconductor interface to achieve a significant on/off ratio in our memristor device.[15] Figure S14b (Supporting Information) presents the optical and corresponding AFM images of the lateral device. By modulating the source-drain current laterally without a back-gate voltage, a hysteresis loop in the I_{ds}–V_{ds} curve is elicited under varying maximum-sweep voltages, as shown in Figure S16 (Supporting Information). The curves exhibit distinct hysteretic windows that progressively widen as the maximum sweep voltage increases. The black arrows in Figure S16a (Supporting Information) illustrate the voltage sweep direction across four stages. Notably, the onset of the hysteresis loop at $V_d = \pm$ 1.8 V indicates the presence of two critical voltages, aligning with the intrinsic polarization switching of the in-plane ferroelectric (Figure S16b, Supporting Information). The hysteresis loop observed in the I_{ds}–V_{ds} curve, which is influenced by an external lateral electric field, suggests the presence of in-plane ferroelectric polarization in 2D BTO. Figure S17 (Supporting Information) illustrates the schematic diagram of the polarization mechanism for in-plane ferroelectricity devices, with double counterclockwise hysteresis distinguishing it from capacitive effects.[37,38]

2.4. DEBT Buffer Layer Release of Strain to Stabilize the BTO Monolayer

Previous evidence indicates that a DEBT buffer layer with a disordered elemental distribution stabilizes the BTO monolayer, facilitating ultrathin in-plane ferroelectricity at a single-unit cell thickness. Maintaining this ferroelectricity is complex, typically influenced by factors such as lattice mismatch-induced phase transitions and strains.[39–42] The ferroelectric polarization of BTO mainly originated from the displacements of Bi^{3+} as well as from the lattice deflection angle, thus emphasizing the impact of strain on in-plane ferroelectricity is crucial. In this light, we analyzed the strain of the DEBT layer and upon BTO nanosheets to investigate the stabilizing mechanism. For comparison, the strain analysis of the DEBT monolayer and BTO bilayer are shown in **Figure** 4b,d, from which it can be seen that the DEBT monolayer has large strain fluctuation, which is related to its disordered chemical element distribution. In contrast, the BTO bilayer grown on the DEBT bilayer exhibits smaller strain fluctuations. Additional detailed side-view HADDF-STEM images and strain analyses (Figure 4e,f) demonstrate that the DEBT monolayer nearest the substrate has the highest strain strength, decreasing gradually in the out-of-plane direction with increased thickness along the *c*-axis. To further examine the variation in lattice parameters, we extracted precise atomic positions from Figure 4e and performed a statistical analysis.[43] As shown in Figure S18 (Supporting Information), near the substrate, the lattice spacing in the c-direction is larger, indicating greater strain fluctuations in this region. As the distance from the substrate increases, the lattice spacing in the c-direction gradually decreases, and strain fluctuations become smaller. We also provide the side-view images of the few-layer BTO and bilayer DEBT, as shown in Figure S19 (Supporting Information). For the few-layer BTO sample, as seen in Figure S19a, the results are consistent with the information presented in Figure 4e. For the ultrathin bilayer DEBT sample, shown in Figure S19 (Supporting Information). Due to the sample's ultrathin nature, it is difficult to avoid wrinkles and bending during operation, making it challenging to capture images along the a-axis. To precisely understand strain variation at the interface, we analyzed the lattice mismatch in the *a*-axis and *b*-axis directions between BTO and the mica substrate, as detailed in Figure S20 (Supporting Information). Compressive strains of 4.27% in the *a*-axis are revealed where (001) planes of the BTO meets (001) plane of the mica. Such mismatches can destabilize the ferroelectric phase, a finding corroborated by structural analyses and strain statistics from overhead views. Introducing a DEBT layer between mica and BTO significantly reduces the interface strain to as low as 0.2%. The DEBT layer effectively mitigates strain, diminishing the intensity between the BTO monolayer and the substrate, thus stabilizing the structure and enabling in-plane ferroelectricity.

Moreover, BTO was reported to suffer from a phase transition to antiferroelectric through intercalation of the Bi/Te layer.[26] The epitaxial growth of the layered antiferroelectric phase was examined using atomically resolved HAADF-STEM (Figure S21, Supporting Information). Detailed FFT and EDS statistics indicated that antiferroelectric BTO nanosheets with five or more layers maintain similar crystal structures. However, in nanosheets with four or fewer layers, a disordered chemical arrangement results in the disappearance of superspots in FFT images (Figure S22, Supporting Information). This suggests that the DEBT layer can achieve a thickness of up to four-unit cells in antiferroelectric BTO nanocrystals. EDS measurements revealed a Bi deficiency in BTO nanosheets with fewer layers, as depicted in Figure S23 (Supporting Information). This deficiency increases as the layer number decreases, both in the ferroelectric and antiferroelectric phases, with the antiferroelectric phase exhibiting a greater Bi deficiency compared to the ferroelectric phase. This observation supports the existence of a disordered chemical arrangement in the DEBT buffer layer.

DFT calculations were used to further explain the stabilization of in-plane ferroelectricity in single unit-cell BTO. The most stable ferroelectric phase of the free-standing BTO monolayer is shown schematically in Figure 4g. The 0.15 Å displacements of

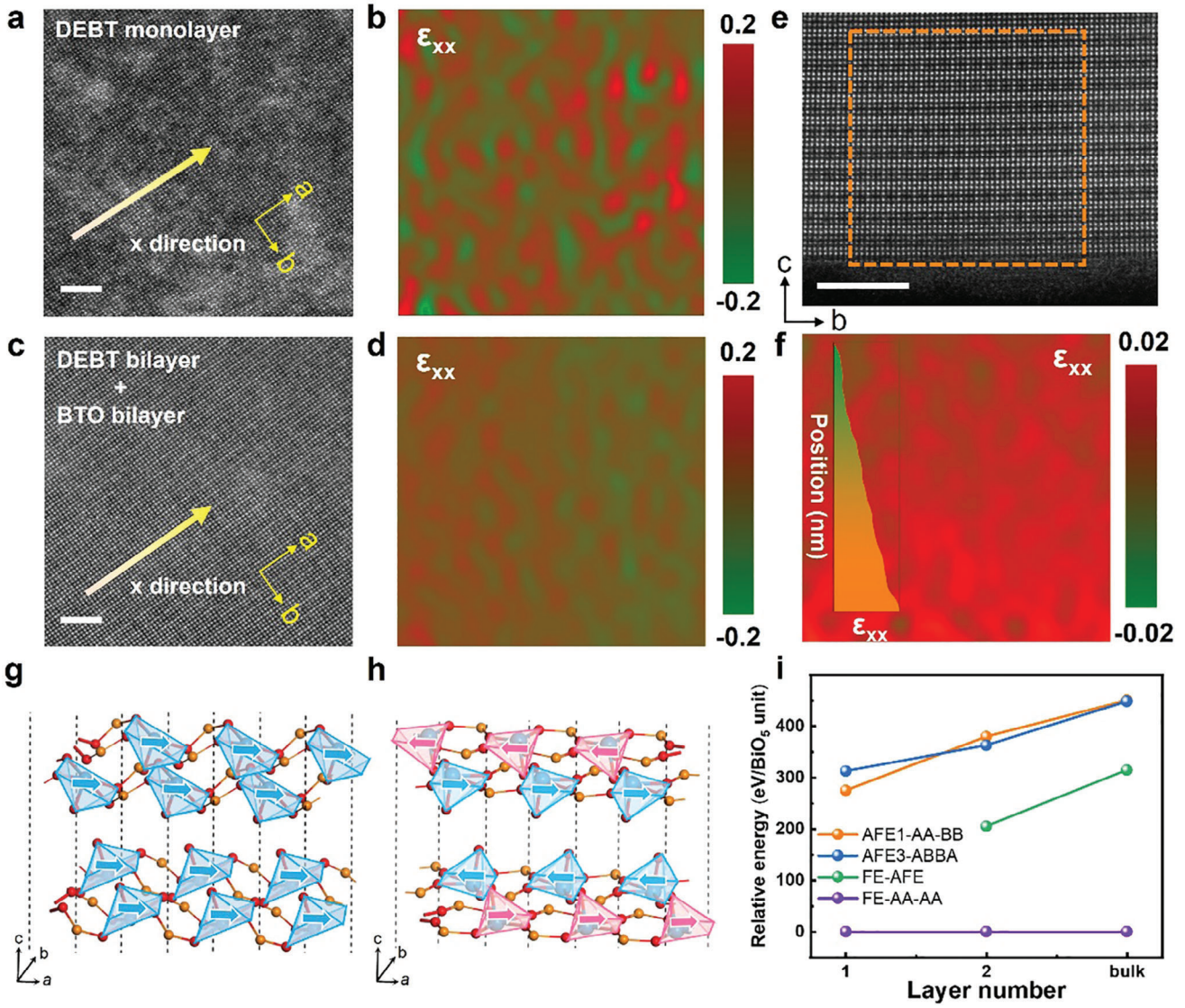

Figure 4. Disordered bismuth tellurite buffer layer promotes ferroelectric monolayer nanosheet generation. a) The HADDF-STEM of the DEBT monolayer and b) corresponding strain along the *c*-axis show a large fluctuation in strain distribution. c) The HADDF-STEM of DEBT monolayer and BTO bilayer along the *c*-axis. d) The corresponding strain in (c) along the *c*-axis shows less fluctuation of strain distribution. e) Atomically resolved HAADF-STEM images of DEBT and BTO multilayer along the *a*-axis. f) The corresponding strain in (e) along the *b*-axis shows a gradient in strain distribution. g) Schematics showing ferroelectric (FE) order, and h) antiferroelectric (AFE1) order in BTO. Light-yellow and orange pyramids represent the BiO_5 cages with polarization pointing along the +a and -a direction, respectively. i) The relative energies of the AFE and FE phases in BTO as a function of the number of layers. Scale bar 5 nm.

surface Bi^{3+} cations along the *a* axis in the BiO_5 cages (marked with pyramids) lead to an in-plane polarization of 5.29 e Å/u.c along the *a* axis (Table S1, Supporting Information), consistent with our experimental PFM observations of the polarization along the *a* axis. The second stable in-plane antiferroelectric phase AFE1 is shown in Figure 4h and can mostly simulate properties of the corresponding paraelectric phase with randomly arranged local polarization directions. As shown in Figure 4i, the ferroelectric phase is always the most stable for free-standing BTO with its thickness reducing from the bulk to the bilayer and then to the monolayer limit. The energy difference between the ferroelectric phase and the antiferroelectric phases decreases with the decreasing number of layers, but is still over 250 meV/BiO_5 in monolayer BTO (Table S1, Supporting Information). The lattice constant *a* of the FE phase (5.52 Å) of the pristine BTO monolayer is very different from that of the antiferroelectric phase (5.27 Å), indicating significant strain tunability. Adapting the AFE1 lattice, which mainly corresponds to a 4.5% compressive strain in the *a* direction and is consistent with the experimentally observed mica-induced epitaxial compressive strain of 4.27% along the *a* axis of the ferroelectric lattice, significantly reduces the energy advantage of the FE phase over the AFE phase to 130 meV per BiO_5. Our calculations indicate that epitaxial compressive and tensile strain along the *a* axis could significantly

reduce the stability of the ferroelectric phase, making the stress release through the DEBT layers crucial to achieving monolayer preparation (Figure S20, Supporting Information).

2.5. Scalable Strategies for Ternary Oxide Synthesis

By relying on our previous modulation of the BTO growth strategy, we found that the controlled growth of a variety of 2D ternary oxide nanosheets can be achieved by modulating the growth kinetics near the growth temperature, in which BiOCl and BiOI can have a similar growth pattern to BTO as shown in Figure S24 (Supporting Information). BiOCl and BiOI nanosheets prefer stacked growth on thinner nanosheets, which opens up the possibility of preparing homogeneous junctions in the vertical direction as well as the creation of molar transitions.

Beyond that, reducing the growth rate near the growth temperature facilitates the formation of ultrathin ternary oxide nanosheets. $M_2Te_3O_8$ (M = Mn, Co, Ni, Cu, Zn), a typical ternary oxide with a lithium-iron ore structure, exhibits complex interactions among spin, charge, and phonon degrees of freedom.[44] However, synthesizing its 2D nanosheets is challenging. By reducing the growth rate near the growth temperature, we successfully synthesized 2D $Ni_2Te_3O_8$ and $Co_2Te_3O_8$ nanosheets on mica substrates. According to Figure S25 (Supporting Information), the $Ni_2Te_3O_8$ nanosheets, owing to their monoclinic crystalline structure, form parallelograms and can reach sizes up to one hundred micrometers. These nanosheets also display a tendency to stack in a particular direction. Raman spectroscopy indicates that the nanosheets differ from the substrate, displaying unique characteristics at a low wavelength of 155.4 $cm.^{-1}$[45] Employing the same method, we have grown $Co_2Te_3O_8$ nanosheets on mica substrates (as depicted in Figure S26, Supporting Information), which also form parallelogram-like shapes and exhibit a similar stacking orientation. Raman spectroscopy shows that these nanosheets feature distinct peaks at low-wave numbers of 110.4 cm^{-1} and 131.7 cm^{-1}, differing from the substrate.[46] This confirms that our buffered growth strategy can be effectively applied to synthesize other 2D ternary oxide nanosheets.

3. Conclusion

In summary, we demonstrate the realization of a buffer layer with a disordered chemical element distribution on a mica substrate. This was achieved by tuning the growth rate of the BTO ternary oxide near the growth temperature, which enabled the further preparation of BTO nanosheets with in-plane ferroelectricity and a single-unit cell thickness. The DEBT buffer layer with two-unit cell thickness reduces the lattice mismatch between the mica substrate and the strictly ordered BTO crystals, stabilizing the BTO monolayer. At a thickness of three units, these nanosheets achieved nearly perfect lattice alignment and demonstrated single-unit cell ferroelectric properties. Theoretical calculations confirmed that DEBT effectively facilitates the formation of BTO monolayers by managing strain and stabilizing ferroelectricity at the single-unit cell level. The spontaneous formation of planar disordered chemical element distribution buffer layers introduces a new growth mechanism for controlling the development of 2D ternary oxide monolayer nanosheets, which holds promise for future applications in 2D ferroelectric electronic devices.

4. Experimental Section

CVD Growth of 2D BTO Nanosheets on Mica: Ultrathin BTO nanosheets were synthesized using a homemade atmospheric-pressure CVD system consisting of a dual-heating zone furnace and a 30 mm diameter quartz tube. In this process, 200 mg of Bi_2O_3 (99.99%, Alfa) powders were combined with a small amount of KI powder and placed in the central region of the furnace. Meanwhile, powders of 100 mg Te (99.999%, Alfa) were positioned in the upstream heating zones. The freshly prepared side of the fluorogold mica substrate ($[KMg_3(AlSi_3O_{10})F_2]$) with atomic leveling was placed facing the mixture source. Prior to initiating the heating processes, the CVD system was carefully sealed, evacuated, and purged with Ar gas to remove all traces of oxygen. The furnace was then heated to 500 °C at a ramp rate of 30 °C min^{-1} and held for 2–5 min to synthesize a DEBT buffer layer, which was then heated to 550 °C–600 °C and held for 10 min to obtain BTO nanosheets. Subsequently, the system was naturally cooled to room temperature. Throughout the entire reaction process, a constant Ar gas flow rate of 200 standard cubic centimeters per minutes (sccm) was maintained.

Characterizations of 2D BTO Nanosheets: The as-grown BTO nanosheets were initially inspected using an optical microscope (Nikon, Eclipse L200N), followed by AFM imaging (Bruker, Dimension Icon) to evaluate their thickness and surface topology. Detailed analyses of the microstructures and compositions were performed using SEM (Hitachi-SU8220) and SEM-EDX. Further characterization of the crystalline structure and phase composition was conducted using XRD (D8 Advance) and Raman spectroscopy (Lab RAM HR800, equipped with a 532 nm laser). Additionally, XPS characterization was also conducted using a ULVAC-PHI instrument (PHI 5000 Versaprobe II), equipped with a 650 µm diameter and 50 eV fluence energy to obtain high-resolution spectra. All analyses utilized an argon-driven oil gun for charge neutralization. To verify the crystal structure, atom arrangement, and elemental mapping of the BTO nanosheets, HAADF-STEM imaging was performed using a Thermo Scientific Themis Z system with an integrated energy-dispersive X-ray detector. The probe's semi-convergence angle was set at 25.1 mrad, while the detector's collection angle ranged from 38 to 200 mrad.

Transfer of 2D BTO Nanosheets: To facilitate the transfer of the as-grown CVD samples, a wet transfer method assisted by hydrofluoric acid (HF) was employed. Initially, the samples were spin-coated with a layer of poly(methyl methacrylate) (PMMA) at a speed of 2000 rpm for 60 s. The coated sample was subsequently baked at 150 °C for a duration of 10 min. Next, an etching process was performed by immersing the PMMA-coated sample into an HF solution with a concentration 5% for a time period of 30 min. The floating PMMA film was then carefully cleaned using distilled water and subsequently transferred onto alternative substrates such as Si/SiO_2, Au foils, or Cu grids. To enhance the interaction between the substrates and the 2D BTO nanosheets, the transferred sample underwent a baking process at a temperature of 75 °C for 15 min. Following this, the PMMA layer was easily removed by immersing the sample in acetone for 10 min.

Device Fabrication and Transport Characterization: The electrodes (Cr/Au) for the two-terminal devices were fabricated using electron-beam lithography (EBL, JBX5500ZA) process, e-beam evaporation technique (Ei-5z), and lift-off processes. Electrical measurements were conducted with a semiconductor characterization system (4200SCS, Keithley).

First-Principles Calculation: Density functional theory (DFT) calculations were conducted using the Vienna Ab-initio Simulation Package (VASP). These calculations employed the generalized gradient approximation (GGA) for the exchange-correlation potential and the projector augmented-wave (PAW) method. A plane wave basis set was utilized throughout the simulation process,[47] and plane wave basis set was utilized throughout the simulation process.[48,49] In VASP calculations, a uniform k-mesh of 4 × 2 × 1 was adopted to sample the first Brillouin zone

of the unit cell of the mono- and few layer structure of BTO. A sufficiently large vacuum layer of over 15 Å was adopted to eliminate imaging interactions with adjacent periods. A kinetic energy cutoff of 700 eV was selected for the plane wave basis set, facilitating the calculations of both geometric and electronic structures. The van der Waals interactions were accounted for using the vdW-DF approach,[50,51] incorporating the optB86b functional for the exchange potential.[52] This method has demonstrated robust performance in accurately describing the structural properties of layered materials.[53,54] The shape and area of each supercell were fully optimized and all atoms were allowed to relax until the residual force per atom was less than 0.01 eV $Å^{-1}$. The in-plane electric polarization was evaluated using the Berry phase method with a non-polar phase chosen as the reference zero.[55] Detailed geometry and polarization properties of BTO can be found in Table S1 (Supporting Information).

Supporting Information

Supporting Information is available from the Wiley Online Library or from the author.

Acknowledgements

The authors acknowledge support from the Key Research and Development Program of Jiangsu Province (Grants No. BK20232009), the China Postdoctoral Science Foundation (Grant No. 2023M742561), the Jiangsu Funding Program for Excellent Postdoctoral Talent, Ministry of Science and Technology (MOST) of China (Grants No. 2023YFA1406500 and 2018YFE0202700), the Jiangsu Province Youth Fund (BK20240478), the National Natural Science Foundation of China (Grants No. 11974422, 12104504, 9477205, 52372055, 52402068 and 52202184), the Strategic Priority Research Program of Chinese Academy of Sciences (Grant No. XDB30000000), Key Research and Development Program of Jiangsu (BK20232009), Basic Research Program of Jiangsu (BK20243006), Basic Research Development Program of SuZhou (SJC2023004), the Fundamental Research Funds for the Central Universities, and the Research Funds of Renmin University of China (Grant No. 22XNKJ30). The authors are grateful for the assistance of SUSTech Core Research Facilities, the technical support for Nano-X from Suzhou Institute of Nano-Tech and Nano-Bionics, Chinese Academy of Sciences (SINANO). All calculations for this study were performed at the Physics Lab of High-Performance Computing (PLHPC) and the Public Computing Cloud (PCC) of Renmin University of China.

Conflict of Interest

The authors declare no conflict of interest.

Author Contributions

Y.L., A.L., and C.W. contributed equally to this work. L.K. and J.L. supervised the project. Y.L. developed and optimized the synthesis method of the sample, conducted Raman, XPS characterizations and wrote the manuscript. A.L. is responsible for the preparation, testing and data analysis of two-terminal FE devices. C.W. and W.J. performed the DFT calculations. M.H. conducted the AFM and STEM characterizations. J.Z., S.W., and L.Y. helped with the spectroscopic characterizations and data analysis. P.Z. helped with KPFM characterizations. G.S., Z.S., L.W., and Y.Z. helped with data analysis. Y.Z. helped with schematic drawing. All authors discussed the results and commented on the manuscript.

Data Availability Statement

The data that support the findings of this study are available from the corresponding author upon reasonable request.

Keywords

bismuth tellurite, buffer layer, ferroelectric materials, single-unit cell, strain engineering

Received: November 6, 2024
Revised: December 12, 2024
Published online:

[1] C. Wang, L. You, D. Cobden, J. Wang, *Nat. Mater.* **2023**, *22*, 542.
[2] J. Gou, H. Bai, X. Zhang, Y. L. Huang, S. Duan, A. Ariando, S. A. Yang, L. Chen, Y. Lu, A. T. S. Wee, *Nature* **2023**, *617*, 67.
[3] A. Jindal, A. Saha, Z. Li, T. Taniguchi, K. Watanabe, J. C. Hone, T. Birol, R. M. Fernandes, C. R. Dean, A. N. Pasupathy, D. A. Rhodes, *Nature* **2023**, *613*, 48.
[4] K. Yasuda, X. Wang, K. Watanabe, T. Taniguchi, P. Jarillo-Herrero, *Science* **2021**, *372*, 1458.
[5] K. Chang, J. Liu, H. Lin, N. Wang, K. Zhao, A. Zhang, F. Jin, Y. Zhong, X. Hu, W. Duan, Q. Zhang, L. Fu, Q.-K. Xue, X. Chen, S.-H. Ji, *Science* **2016**, *353*, 274.
[6] R. Berdan, T. Marukame, K. Ota, M. Yamaguchi, M. Saitoh, S. Fujii, J. Deguchi, Y. Nishi, *Nat. Electron.* **2020**, *3*, 259.
[7] S. Kamaei, X. Liu, A. Saeidi, Y. Wei, C. Gastaldi, J. Brugger, A. M. Ionescu, *Nat. Electron.* **2023**, *6*, 658.
[8] R. Bian, R. He, E. Pan, Z. Li, G. Cao, P. Meng, J. Chen, Q. Liu, Z. Zhong, W. Li, F. Liu, *Science* **2024**, *385*, 57.
[9] K. Yasuda, E. Zalys-Geller, X. Wang, D. Bennett, S. S. Cheema, K. Watanabe, T. Taniguchi, E. Kaxiras, P. Jarillo-Herrero, R. Ashoori, *Science* **2024**, *385*, 53.
[10] T. H. Yang, B.-W. Liang, H.-C. Hu, F.-X. Chen, S.-Z. Ho, W.-H. Chang, L. Yang, H.-C. Lo, T.-H. Kuo, J.-H. Chen, P.-Y. Lin, K. B. Simbulan, Z.-F. Luo, A. C. Chang, Y.-H. Kuo, Y.-S. Ku, Y.-C. Chen, Y.-J. Huang, Y.-C. Chang, Y.-F. Chiang, T.-H. Lu, M.-H. Lee, K.-S. Li, M. Wu, Y.-C. Chen, C.-L. Lin, Y.-W. Lan, *Nat. Electron.* **2023**, *7*, 29.
[11] F. Liu, L. You, K. L. Seyler, X. Li, P. Yu, J. Lin, X. Wang, J. Zhou, H. Wang, H. He, S. T. Pantelides, W. Zhou, P. Sharma, X. Xu, P. M. Ajayan, J. Wang, Z. Liu, *Nat. Commun.* **2016**, *7*, 12357.
[12] W. Li, X. Zhang, J. Yang, S. Zhou, C. Song, P. Cheng, Y.-Q. Zhang, B. Feng, Z. Wang, Y. Lu, K. Wu, L. Chen, *Nat. Commun.* **2023**, *14*, 2757.
[13] S. Yuan, X. Luo, H. L. Chan, C. Xiao, Y. Dai, M. Xie, J. Hao, *Nat. Commun.* **2019**, *10*, 1775.
[14] P. Man, L. Huang, J. Zhao, T. H. Ly, *Chem. Rev.* **2023**, *123*, 10990.
[15] N. Higashitarumizu, H. Kawamoto, C.-J. Lee, B.-H. Lin, F.-H. Chu, I. Yonemori, T. Nishimura, K. Wakabayashi, W.-H. Chang, K. Nagashio, *Nat. Commun.* **2020**, *11*, 2728.
[16] Y. Zhou, D. Wu, Y. Zhu, Y. Cho, Q. He, X. Yang, K. Herrera, Z. Chu, Y. Han, M. C. Downer, H. Peng, K. Lai, *Nano Lett.* **2017**, *17*, 5508.
[17] W. Han, X. Zheng, K. Yang, C. S. Tsang, F. Zheng, L. W. Wong, K. H. Lai, T. Yang, Q. Wei, M. Li, W. F. Io, F. Guo, Y. Cai, N. Wang, J. Hao, S. P. Lau, C.-S. Lee, T. H. Ly, M. Yang, J. Zhao, *Nat. Nanotechnol.* **2022**, *18*, 55.
[18] P. Wang, Y. Zhao, R. Na, W. Dong, J. Duan, Y. Cheng, B. Xu, D. Kong, J. Liu, S. Du, C. Zhao, Y. Yang, L. Lv, Q. Hu, H. Ai, Y. Xiong, V. S. Stolyarov, S. Zheng, Y. Zhou, F. Deng, J. Zhou, *Adv. Mater.* **2024**, *36*, 2400655.
[19] L. A. Bursill, P. J. Lin, *Nature* **1984**, *311*, 550.
[20] C. Lichtensteiger, J.-M. Triscone, J. Junquera, P. Ghosez, *Phys. Rev. Lett.* **2005**, *94*, 047603.
[21] Y. Yun, P. Buragohain, M. Li, Z. Ahmadi, Y. Zhang, X. Li, H. Wang, J. Li, P. Lu, L. Tao, H. Wang, J. E. Shield, E. Y. Tsymbal, A. Gruverman, X. Xu, *Nat. Mater.* **2022**, *21*, 903.

[22] Q. Yang, J. Hu, Y.-W. Fang, Y. Jia, R. Yang, S. Deng, Y. Lu, O. Dieguez, L. Fan, D. Zheng, X. Zhang, Y. Dong, Z. Luo, Z. Wang, H. Wang, M. Sui, X. Xing, J. Chen, J. Tian, L. Zhang, *Science* **2023**, *379*, 1218.
[23] S. S. Cheema, D. Kwon, N. Shanker, R. dos Reis, S.-L. Hsu, J. Xiao, H. Zhang, R. Wagner, A. Datar, M. R. McCarter, C. R. Serrao, A. K. Yadav, G. Karbasian, C.-H. Hsu, A. J. Tan, L.-C. Wang, V. Thakare, X. Zhang, A. Mehta, E. Karapetrova, R. V. Chopdekar, P. Shafer, E. Arenholz, C. Hu, R. Proksch, R. Ramesh, J. Ciston, S. Salahuddin, *Nature* **2020**, *580*, 478.
[24] D. Ji, S. Cai, T. R. Paudel, H. Sun, C. Zhang, L. Han, Y. Wei, Y. Zang, M. Gu, Y. Zhang, W. Gao, H. Huyan, W. Guo, D. Wu, Z. Gu, E. Y. Tsymbal, P. Wang, Y. Nie, X. Pan, *Nature* **2019**, *570*, 87.
[25] S. S. Cheema, N. Shanker, S.-L. Hsu, Y. Rho, C.-H. Hsu, V. A. Stoica, Z. Zhang, J. W. Freeland, P. Shafer, C. P. Grigoropoulos, J. Ciston, S. Salahuddin, *Science* **2022**, *376*, 648.
[26] M. Han, C. Wang, K. Niu, Q. Yang, C. Wang, X. Zhang, J. Dai, Y. Wang, X. Ma, J. Wang, L. Kang, W. Ji, J. Lin, *Nat. Commun.* **2022**, *13*, 5903.
[27] T. Jurca, M. J. Moody, A. Henning, J. D. Emery, B. Wang, J. M. Tan, T. L. Lohr, L. J. Lauhon, T. J. Marks, *Angew. Chem., Int. Ed.* **2017**, *56*, 4991.
[28] M.-C. Chang, P.-H. Ho, M.-F. Tseng, F.-Y. Lin, C.-H. Hou, I. K. Lin, H. Wang, P.-P. Huang, C.-H. Chiang, Y.-C. Yang, I. T. Wang, H.-Y. Du, C.-Y. Wen, J.-J. Shyue, C.-W. Chen, K.-H. Chen, P.-W. Chiu, L.-C. Chen, *Nat. Commun.* **2020**, *11*, 3682.
[29] G. Zhou, R. Younas, T. Sun, G. Harden, Y. Li, A. J. Hoffman, C. L. Hinkle, *ACS Nano* **2022**, *16*, 19385.
[30] H. Amano, *Angew. Chem., Int. Ed.* **2015**, *54*, 7764.
[31] C. Shou, T. Yang, A. Almujtabi, T. Yang, Y. Li, Q. S. Mahmud, M. Xu, J.-G. Zheng, J. Liu, *Appl. Phys. Lett.* **2023**, *122*, 212101.
[32] K. V. Agarkov, L. Y. Sadovskaya, *Acta Phys. Pol. A* **2018**, *133*, 940.
[33] K. V. Domoratskii, V. I. Pastukhov, A. Y. Kudzin, L. Y. Sadovskaya, V. M. Rizak, V. A. Stefanovich, *Phys. Solid State* **2000**, *42*, 1443.
[34] B. Chen, X. Wang, J. Li, Q. Xiong, C. Zhang, *J. Mater. Chem. C* **2018**, *6*, 10435.
[35] R. Montenegro, Z. V. Fabris, D. A. Capovilla, I. de Oliveira, J. Frejlich, J. F. Carvalho, *Opt. Mater.* **2019**, *94*, 398.
[36] J. Jang, S.-Y. Choi, *Microstructures* **2024**, *4*, 2024016.
[37] X. Xu, T. Zhong, N. Zuo, Z. Li, D. Li, L. Pi, P. Chen, M. Wu, T. Zhai, X. Zhou, *ACS Nano* **2022**, *16*, 8141.
[38] M. Yuan, B. Zhang, J. Cai, J. Zhang, Y. Lu, S. Qiao, K. Cao, H. Deng, Q. Ji, *Carbon Neutralization* **2024**, *3*, 700.
[39] M. Wu, Z. Lou, C. M. Dai, T. Wang, J. Wang, Z. Zhu, Z. Xu, T. Sun, W. Li, X. Zheng, X. Lin, *Adv. Mater.* **2023**, *35*, 2300450.
[40] R. Xu, K. J. Crust, V. Harbola, R. Arras, K. Y. Patel, S. Prosandeev, H. Cao, Y. T. Shao, P. Behera, L. Caretta, W. J. Kim, A. Khandelwal, M. Acharya, M. M. Wang, Y. Liu, E. S. Barnard, A. Raja, L. W. Martin, X. W. Gu, H. Zhou, R. Ramesh, D. A. Muller, L. Bellaiche, H. Y. Hwang, *Adv. Mater.* **2023**, *35*, 2210562.
[41] S. Hazra, T. Schwaigert, A. Ross, H. Lu, U. Saha, V. Trinquet, B. Akkopru-Akgun, B. Z. Gregory, A. Mangu, S. Sarker, T. Kuznetsova, S. Sarker, X. Li, M. R. Barone, X. Xu, J. W. Freeland, R. Engel-Herbert, A. M. Lindenberg, A. Singer, S. Trolier-McKinstry, D. A. Muller, G. M. Rignanese, S. Salmani-Rezaie, V. A. Stoica, A. Gruverman, L. Q. Chen, D. G. Schlom, V. Gopalan, *Adv. Mater.* **2024**, *3*, 2408664.
[42] J. Mao, J. He, W. F. Io, F. Guo, Z. Wu, M. Yang, J. Hao, *ACS Nano* **2024**, *18*, 30360.
[43] T. Li, S. Deng, H. Liu, J. Chen, *Chem. Rev.* **2024**, *124*, 7045.
[44] C. R. Feger, G. L. Schimek, J. W. Kolis, *J. Solid State Chem.* **1999**, *143*, 246.
[45] A. Tiwari, D. C. Kakarla, B. Poojitha, P. Sahoo, H. L. Liu, A. Dixit, C. W. Wang, T. W. Yen, M. J. Hsieh, J. Y. Lin, J. Krishnamurthy, Y. C. Lai, H. Chou, T. W. Kuo, A. Pal, H. D. Yang, *Phys. Rev. B* **2023**, *108*, 075113.
[46] N. Li, B. Manoun, Y. Tamraoui, Q. Zhang, H. Dong, Y. Xiao, P. Chow, P. Lazor, X. Lü, Y. Wang, W. Yang, *Phys. Rev. B* **2019**, *99*, 245125.
[47] P. E. Blöchl, *Phys. Rev. B* **1994**, *50*, 17953.
[48] G. Kresse, J. Furthmüller, *Comput. Mater. Sci.* **1996**, *6*, 15.
[49] G. Kresse, J. Furthmüller, *Phys. Rev. B* **1996**, *54*, 11169.
[50] M. Dion, H. Rydberg, E. Schröder, D. C. Langreth, B. I. Lundqvist, *Phys. Rev. Lett.* **2004**, *92*, 246401.
[51] K. Lee, É. D. Murray, L. Kong, B. I. Lundqvist, D. C. Langreth, *Phys. Rev. B* **2010**, *82*, 081101.
[52] J. Klimeš, D. R. Bowler, A. Michaelides, *Phys. Rev. B* **2011**, *83*, 195131.
[53] J. Qiao, Y. Pan, F. Yang, C. Wang, Y. Chai, W. Ji, *Sci. Bull.* **2018**, *63*, 159.
[54] Z.-X. Hu, X. Kong, J. Qiao, B. Normand, W. Ji, *Nanoscale* **2016**, *8*, 2740.
[55] R. D. King-Smith, D. Vanderbilt, *Phys. Rev. B* **1993**, *47*, 1651.